

Negative-Temperature Onsager Vortex Clusters in a Quantum Fluid

Guillaume Gauthier,¹ Matthew T. Reeves,² Xiaquan Yu,³ Ashton S. Bradley,³ Mark Baker,¹ Thomas A. Bell,¹ Halina Rubinsztein-Dunlop,¹ Matthew J. Davis,^{1,2} and Tyler W. Neely¹

¹*Australian Research Council Centre of Excellence for Engineered Quantum Systems, School of Mathematics and Physics, University of Queensland, St. Lucia, QLD 4072, Australia.*

²*Australian Research Council Centre of Excellence in Future Low-Energy Electronics Technologies, School of Mathematics and Physics, University of Queensland, St Lucia, QLD 4072, Australia.*

³*Department of Physics, Centre for Quantum Science, and Dodd-Walls Centre for Photonic and Quantum Technologies, University of Otago, Dunedin, New Zealand.*

(Dated: April 27, 2022)

Turbulence in classical fluids is a ubiquitous non-equilibrium phenomenon, yet a complete theoretical description for turbulent flow remains a challenging problem. A useful simplification for ideal two-dimensional (2D) fluids is to describe the turbulent flow with long-range-interacting point vortices [1–3], each possessing quantised circulation. In 1949, Onsager [4] applied statistical mechanics to determine the equilibria of this model. He showed that at sufficiently high energies, like-circulation vortices preferentially aggregate into large-scale clusters, and are characterised by a negative absolute temperature. Onsager’s theory has been highly influential [5, 6], providing understanding of diverse quasi-2D systems such as turbulent soap films [7], guiding-centre plasmas [8], and self-gravitating systems [9]. It also predicts the striking tendency of 2D turbulence to spontaneously form large-scale, long-lived vortices — Jupiter’s Great Red Spot is a well-known example [10]. However, Onsager’s theory doesn’t quantitatively apply to classical fluids where vorticity is continuous, and experimental systems demonstrating Onsager’s point-vortex statistical mechanics have remained elusive. Here we realise high energy, negative-temperature vortex clusters in a uniform superfluid Bose-Einstein condensate. Our results confirm Onsager’s prediction of negative temperature clustered phases of quantum vortices, and demonstrate the utility of point-vortex statistical mechanics in 2D quantum fluids. This work opens future directions for the study of turbulent dynamics and we anticipate exploring the entire phase diagram of 2D quantum vortices, including the formation of clusters from 2D quantum turbulence [11–13].

Throughout nature the competition between energy and entropy generally means that higher energy states are increasingly disordered. By contrast, an isolated system with a finite phase space becomes more ordered above a certain energy [14], resulting in a negative absolute temperature state. One example is a system of N point vortices in an ideal two-dimensional fluid. Here the kinetic energy of the fluid flow can be recast into a particle-like interaction energy, depending on the relative vortex positions. In an uniform fluid, it has the form

$$H = -\frac{\rho_0}{4\pi} \sum_{i \neq j} \Gamma_i \Gamma_j \ln |\mathbf{r}_i - \mathbf{r}_j|, \quad (1)$$

where ρ_0 is the fluid density and Γ_i is the circulation of a vortex at position \mathbf{r}_i . The peculiar feature of Eq. (1) is that it contains only position information; the presence of a boundary [1] modifies the precise form of the interaction (see Methods), but does not alter this essential property. It follows that when the fluid is confined by a boundary, the available phase space becomes bounded by the area of the container [4].

The phases of a neutral system ($N_{\pm} = N/2$, $\Gamma_i = \pm\Gamma$) of N vortices in an elliptical domain are shown schematically in Fig. 1. Equilibrium states are characterized by their entropy $S(E)$, which measures the possible configurations of vortices for a given energy E . Their Boltzmann temperature is given by the inverse slope of this quantity: $T = (\partial S / \partial E)^{-1}$. The lowest energy, positive temperature phase ($T > 0$) consists of weakly interacting bound vortex-antivortex pairs (Fig. 1a). At higher energy, the vortex positions are essentially random and uncorrelated (Fig. 1b), characteristic of a state with infinite temperature ($T = \pm\infty$). At still higher energies, negative slope implies temperature below zero ($T < 0$), and vortices begin to form small, same-sign clusters. As the energy of the system

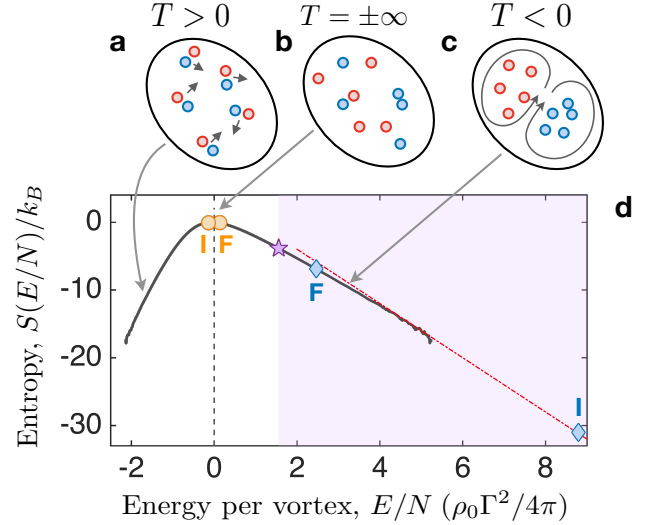


FIG. 1. Equilibrium states of point vortices in a bounded domain. **a**, Small positive temperatures exhibit vortex-antivortex pairing. **b**, States near $T = \pm\infty$ have uncorrelated vortex positions. **c**, The negative temperature regime contains giant Onsager vortex clusters. **d**, Entropy vs. energy curve for a neutral vortex gas. Markers show the approximate initial (I) and final (F) vortex energies for the grid stir (circles) and paddle stir (diamonds) scenarios in this work (see text). The purple star indicates the onset of the clustering transition; energies above this point exhibit Onsager vortex clusters (shaded region). The red line indicates the asymptotic slope at high energies (see text).

continues to increase, a critical temperature T_c is reached [15], where the vortex distribution then begins to polarise, gradually forming two giant clusters of same-circulation vortices –

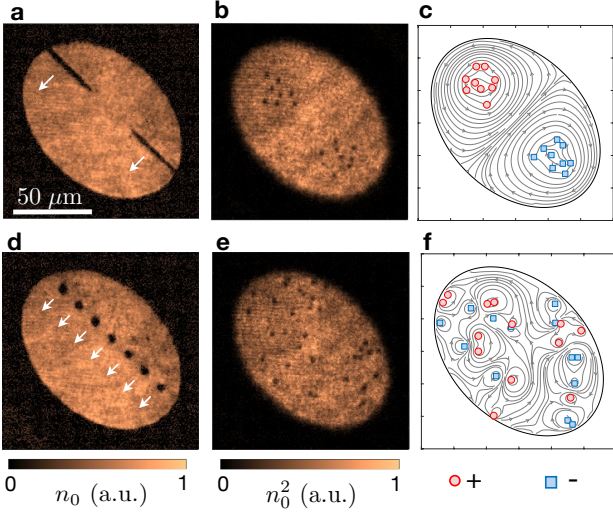


FIG. 2. **Vortex injection results.** **a**, In situ image of the trapped BEC, showing the paddle stirrers partway through the cluster-injection sweep. **b**, A 3 ms time-of-flight Faraday image directly after the paddle sweep clearly resolves injected vortices (see Methods), showing the presence of Onsager vortex clusters. **c**, Simulation of the paddle sweep showing velocity contours, with the location and circulations of the vortices indicated, demonstrating the injection of a clustered vortex dipole. **d,e,f**, As for **a,b,c**, but where a low-energy vortex dipole gas is injected by sweeping a grid of barriers through the BEC.

a giant vortex dipole (Fig. 1c). At the highest energies these clusters spatially contract, forming a maximally-polarised supercondensate [16] comprised of two tightly bound clusters of $N/2$ same-circulation vortices. In the supercondensate limit the entropy-energy curve has an approximately linear slope, implying a nonzero supercondensate temperature T_s (Fig. 1d).

With weak coupling to sound modes, and kinetic energy primarily contained in the vortex flow, a uniform 2D Bose-Einstein condensate (BEC) provides a close realisation of the point-vortex model in a bounded domain [17, 18]. However, in the presence of dissipation, same-circulation vortices drift apart, lowering the energy. Although small transient clusters have been observed in BEC [19–21], attempts to create Onsager vortex clusters must overcome this energy damping. Furthermore, to retain vortices it is necessary to avoid the annihilation of vortex-antivortex pairs that dominates the vortex dipole regime [12], and avoid vortex losses that become significant for inhomogeneous superfluids [22]. If overall dissipation is weak enough, it has been proposed that vortex clusters may form an almost isolated subsystem able to thermalise and store large energy per vortex [11, 23], suggesting the experimental feasibility of studying the negative-temperature clustered phase of quantum vortices. The physical realisation of such states has remained an open question since Onsager’s seminal work of 1949 [4].

Here we work with a planar ^{87}Rb Bose-Einstein condensate confined to a hard-walled elliptical trap with major and minor axis $\{2a, 2b\} = \{120\text{ }\mu\text{m}, 85\text{ }\mu\text{m}\}$ (see Methods). While the BEC itself is three-dimensional, it is two-dimensional for vortex dynamics due to the large energy required to excite Kelvin waves [24].

We inject Onsager vortex clusters into the BEC using a

“double-paddle” whereby two thin barriers are swept along the edges of the trap as illustrated in Fig. 2a. This produces separate clusters of like-circulation quantised vortices, in qualitative agreement with the behaviour expected from a classical fluid[25, 26]. The result is the injection of vortex clusters that settle on the major axis [27] and are easily visible following a short 3 ms time-of-flight expansion, Fig. 2b. We contrast these results with a grid of barriers swept through the BEC, which injects a similar number of vortices but with lower vortex energy, as shown in Fig. 2d,e. The results of Gross-Pitaevskii equation (GPE) simulations quantitatively modelling both sweeps (see Methods) are shown for comparison in Fig. 2c,f, also see Supplementary Videos M1 and M2.

We demonstrate the metastability of the vortex clusters by measuring the spatial distribution of the vortices, at one-second intervals, up to ten seconds of hold time following vortex injection. Figure 3a displays the vortex position histogram of all samples for the paddle sweep, resulting in two clearly distinct clusters containing an average of nine vortices (see Supplementary Video M3 for individual time steps). By contrast, the same analysis for the grid sweep in Fig. 3b shows a near uniform distribution of vortices, as expected near $T = \pm\infty$. Figures 3c,d show the results of analysis of the GPE simulations of both barrier sweeps, where the distribution of the individual positive (negative) vortices are denoted by σ_+ (σ_-). In addition, Fig. 3e compares the total number of vortices as a function of time for the two sweeps in comparison with GPE simulations. The vortex number for the paddle sweep shows no decay in 10 s, while the grid sweep loses 60% of the vortices in this time to vortex annihilation and edge losses. Figure 3f plots the vortex nearest-neighbour distance ℓ normalised by \sqrt{N} and BEC healing length ξ for both cases, which increases with time for the injected Onsager clusters, and approaches the value expected for a uniform distribution at the end of the hold time. By contrast, the grid stir stays quasi-constant near the value expected for a random distribution, suggesting a balance between competing processes of annihilation-driven evaporative heating [11] and dissipation.

One of the limitations of our BEC apparatus is that we currently do not determine the circulations of the vortices. They can instead be inferred from the position of the vortices about the minor axis of the ellipse, which is confirmed by the numerical simulations (see Methods). From these data we can estimate the energy of the experimental vortex configurations as a function of time using the point-vortex model, and this is plotted in Fig. 3g. Despite a gradual decay of the energy, the system remains deep within the negative temperature region for the entire 10s hold time. The decay is due to a combination of the finite lifetime of the condensate ($\tau = 28 \pm 2$ s), and a residual thermal fraction of $\sim 30\%$, resulting in the damping of the energy of the vortex configuration. This conclusion is supported by GPE simulations with phenomenological damping included, which are in excellent agreement with experimental observations (see Fig. 3g). The grid swept case in the simulations shows a small increase in energy per vortex over the hold time, due to the annihilation of low energy vortex-antivortex pairs [11]. Without vortex circulation detection [28], this is not observed in the experiment. For reference, we show the initial and final energies of the grid and paddle stirs, as determined by the GPE simulations, in Fig. 1d. For the paddle stir, as the estimated energy decreases, Fig. 1d indicates increasing entropy, as is character-

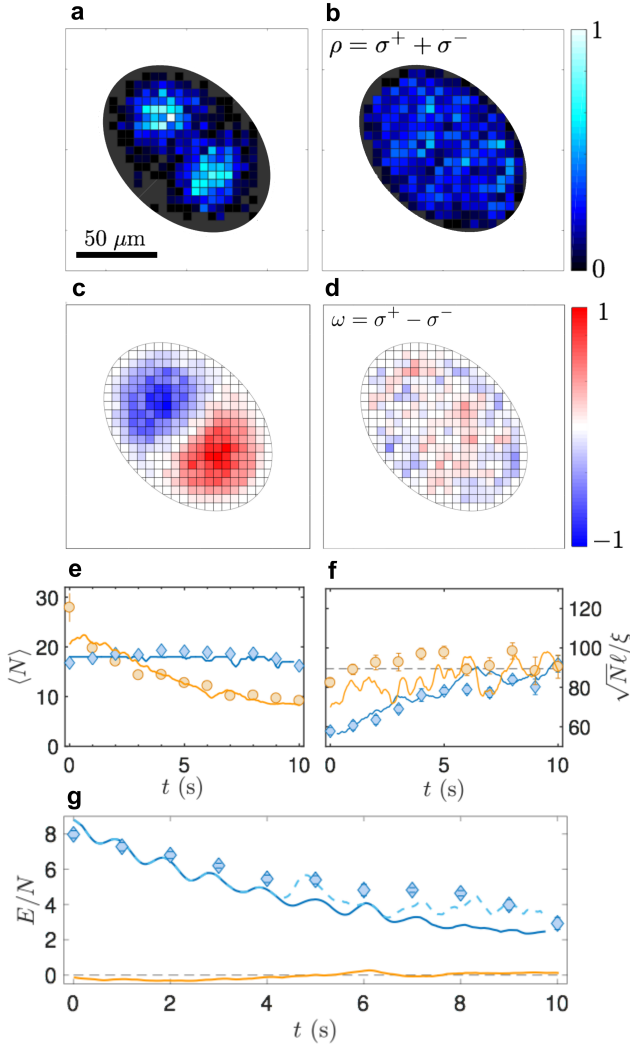


FIG. 3. **Evidence of Onsager vortex cluster metastability.** Experimental (unsigned) vortex density histograms $\rho = \sigma^+ + \sigma^-$ for **a**, paddle and **b**, grid sweeps, respectively. The data are collected following hold times of $t = 0\text{s}, 1\text{s}, 2\text{s}, \dots, 10\text{s}$, with 10 samples at each time (110 samples total). **c**, **d**, Corresponding GPE simulation (signed) vorticity histograms $\omega = \sigma^+ - \sigma^-$ time averaged over 0–10 s. **e**, **f**, Experimental average vortex number $\langle N \rangle$ and number-weighted nearest neighbour distance $\sqrt{N}l/\xi$ vs. hold time for the paddle sweep (blue diamonds) and grid sweep (orange circles). The horizontal dashed line in **f** shows the expected value for a random distribution. GPE simulation results are shown as solid lines of the same colour. **g**, Experimental point-vortex energy (blue diamonds) compared with the point-vortex energy calculated from vortex locations in GPE simulations. Blue solid line: exact point vortex energy. Blue dashed line: estimated energy from applying the experimental protocol to the GPE data. The black horizontal dotted line indicates the energy of the state with $T \pm \infty$, while the orange line indicates the energy of the grid-swept case.

istic of a negative temperature state. For the simulated grid stir, annihilations allow the systems to transition from the positive to negative temperature region.

Further analyses confirm the presence of a clustered Onsager vortex state. The clustered phase can be characterised by a macroscopic dipole moment [15], $D \equiv N^{-1} |\sum_i \kappa_i \mathbf{r}_i|$. This quantity increases continuously with increasing energy,

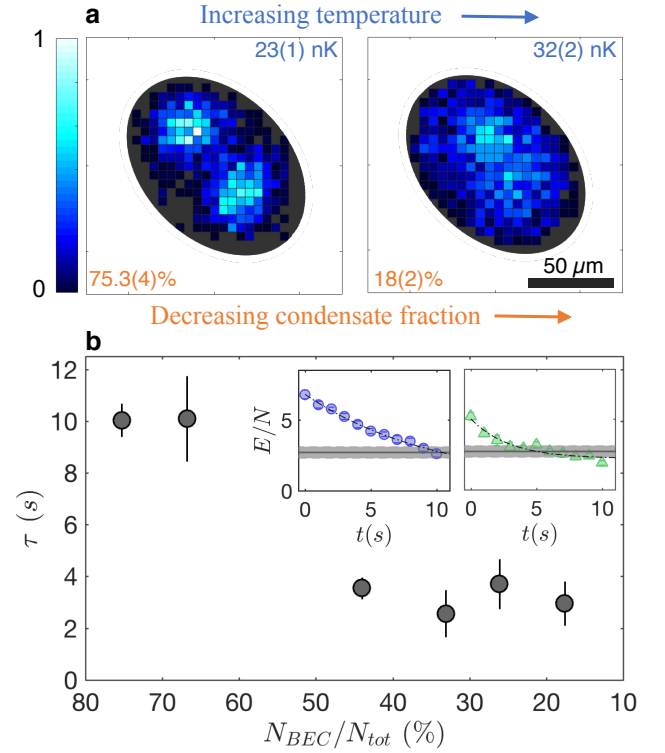


FIG. 4. **Metastability of Onsager vortex clusters with decreased BEC fraction.** **a**, Cumulative vortex histograms over a 10 second hold show more rapid disintegration of the Onsager vortex clusters, see Supplementary Fig. S2 for cumulative histograms for the full set of condensate fractions explored, and Supplementary Fig. S4 for the histograms immediately following the sweep. **b**, The lifetime of the vortex energy as a function of BEC fraction. (inset) The decay of the vortex energy for the largest (blue circles) and smallest (green triangles) condensate fractions. The shaded region indicates the circulation allocation algorithm bounds (see Methods), and fits to an offset exponential decay are shown with dash-dot lines, determining the lifetime.

reaching a maximum value at the supercondensate, with clusters located symmetrically along the major axis at distance $\pm d$ from the ellipse centre. The dipole moment is thus bounded by $D \leq d$. For our trap configuration we predict $d \simeq 0.47a$ (see Methods), while the experimental vortex position data for the final state gives $D_{\text{exp}} \simeq 0.40a$, indicating that our experiment remains deep in the clustered phase. Moreover our analysis shows that the clustering transition occurs at a critical temperature $T_c \simeq -0.62T_0$ (see Methods), while supercondensation [15] occurs at $T_s = -0.5T_0$. Evaluating the point-vortex Hamiltonian for the experimental data of the final state, we estimate the temperature $T_{\text{exp}} = T(E_{\text{exp}})$, and find $T_{\text{exp}} \simeq -0.57T_0$, in between the clustering and supercondensation temperatures.

To characterise the decay of the Onsager vortex clusters, we inject clusters for a range of smaller condensate fractions and correspondingly higher BEC temperatures, while maintaining the same injected vortex number (See Supplementary Fig. S5). Cumulative vortex histograms for the largest and smallest condensate fractions are shown in Fig. 4a, and show diminished clusters with decreasing condensate fraction. We observe a reduction in the cluster decay time τ as the condensate fraction decreases, as shown in Fig. 4b. The scaled energy loss curves

for these two cases are compared in the inset of Fig. 4b, and horizontal shaded regions represent confidence intervals for our energy estimation (see Methods).

In summary we have reported the creation and characterisation of the clustered phase of quantum vortices predicted by Onsager's statistical mechanics of point-vortices in a bounded domain [4]. Beyond the point-vortex model, we have identified vortex-antivortex pair annihilation and residual thermal damping of the superfluid as sources of relatively weak dissipation. The precise control of the trapping potential in our experiment enables a broad range of stirring and trapping configurations, opening the door to further studies of the vortex clustering phase transition [11, 15, 23], and of fully developed quantum turbulence confined to two dimensions. Emerging tools for precision characterisation, including vortex circulation detection [12], momentum spectroscopy [29], and correlation functions [25, 30], can be expected to provide further insights into the role of coherent structures in 2D quantum turbulence.

We note that the group of K. Helmersson has independently observed negative absolute temperature vortex states in a similar system, along with signatures of evaporative heating by vortex-antivortex annihilation [28].

Acknowledgements We thank B.P. Anderson, L. Williamson, B. Blakie, K. Helmersson, T. Simula, S. Johnstone, A. Groszek, and G. Milburn for comments on the manuscript. Funding was provided by the ARC Centre of Excellence for Engineered Quantum Systems (project number CE1101013), and ARC Discovery Projects grant DP160102085. This research was also partially supported by the Australian Research Council Centre of Excellence in Future Low-Energy Electronics Technologies (project number CE170100039) and funded by the Australian Government. T.A.B. and G.G. acknowledge the support of an Australian Government Research and Training Program Scholarship.

-
- [1] C. C. Lin, P. Nat. Acad. Sci. **27**, 570 (1941).
 - [2] E. A. Novikov, Zhurnal Eksperimental'noi i Teoreticheskoi Fiziki **68**, 1868 (1976).
 - [3] H. Aref, Annu. Rev. Fluid Mech. **15**, 345 (1983).
 - [4] L. Onsager, Il Nuovo Cimento (1943-1954) **6**, 279 (1949).
 - [5] R. H. Kraichnan, The Physics of Fluids **10**, 1417 (1967).
 - [6] D. Montgomery and G. Joyce, Phys. Fluids **17**, 1139 (1974).
 - [7] M. A. Rutgers, Phys. Rev. Lett. **81**, 2244 (1998).
 - [8] R. A. Smith and T. M. O'Neil, Physics of Fluids B: Plasma Physics **2**, 2961 (1990).
 - [9] J. Binney and S. Tremaine, *Galactic dynamics* (Princeton University Press, 2011).
 - [10] J. Sommeria, S. D. Meyers, and H. L. Swinney, Nature **331**, 689 (1988).
 - [11] T. Simula, M. J. Davis, and K. Helmersson, Phys. Rev. Lett. **113**, 165302 (2014).
 - [12] S. W. Seo, B. Ko, J. H. Kim, and Y. Shin, Sci. Rep. **7**, 4587 (2017).
 - [13] M. T. Reeves, T. P. Billam, B. P. Anderson, and A. S. Bradley, Phys. Rev. Lett. **110**, 104501 (2013).
 - [14] S. Braun, J. P. Ronzheimer, M. Schreiber, S. S. Hodgman, T. Rom, I. Bloch, and U. Schneider, Science **339**, 52 (2013).
 - [15] X. Yu, T. P. Billam, J. Nian, M. T. Reeves, and A. S. Bradley, Physical Review A **94**, 023602 (2016).
 - [16] R. H. Kraichnan, J. Fluid Mech. **67**, 155 (1975).
 - [17] A. L. Fetter, Phys. Rev. **151**, 100 (1966).
 - [18] A. Lucas and P. Surówka, Phys. Rev. A **90**, 053617 (2014).
 - [19] T. W. Neely, E. C. Samson, A. S. Bradley, M. J. Davis, and B. P. Anderson, Phys. Rev. Lett. **104**, 160401 (2010).
 - [20] T. W. Neely, A. S. Bradley, E. C. Samson, S. J. Rooney, E. M. Wright, K. J. H. Law, R. Carretero-González, P. G. Kevrekidis, M. J. Davis, and B. P. Anderson, Phys. Rev. Lett. **111**, 235301 (2013).
 - [21] W. J. Kwon, J. H. Kim, S. W. Seo, and Y. Shin, Phys. Rev. Lett. **117**, 245301 (2016).
 - [22] A. J. Groszek, T. P. Simula, D. M. Paganin, and K. Helmersson, Phys. Rev. A **93**, 043614 (2016).
 - [23] T. P. Billam, M. T. Reeves, B. P. Anderson, and A. S. Bradley, Phys. Rev. Lett. **112**, 145301 (2014).
 - [24] S. J. Rooney, P. B. Blakie, B. P. Anderson, and A. S. Bradley, Phys. Rev. A **84**, 023637 (2011).
 - [25] A. C. White, C. F. Barenghi, and N. P. Proukakis, Phys. Rev. A **86**, 013635 (2012).
 - [26] G. W. Stagg, N. G. Parker, and C. F. Barenghi, J. Phys. B: At. Mol. Opt. Phys. **47**, 095304 (2014).
 - [27] J. Esler and T. Ashbee, J. Fluid Mech. **779**, 275 (2015).
 - [28] S. Johnstone, A. J. Groszek, P. T. Starkey, C. J. Billington, T. P. Simula, and K. Helmersson, submitted (2017).
 - [29] M. T. Reeves, T. P. Billam, B. P. Anderson, and A. S. Bradley, Phys. Rev. A **89**, 053631 (2014).
 - [30] A. Skaugen and L. Angheluta, Phys. Rev. E **93**, 042137 (2016).
 - [31] G. Gauthier, I. Lenton, N. M. Parry, M. Baker, M. Davis, H. Rubinsztein-Dunlop, and T. Neely, Optica **3**, 1136 (2016).
 - [32] Y.-J. Lin, A. R. Perry, R. L. Compton, I. B. Spielman, and J. V. Porto, Phys. Rev. A **79**, 063631 (2009).
 - [33] K. E. Wilson, Z. L. Newman, J. D. Lowney, and B. P. Anderson, Phys. Rev. A **91**, 023621 (2015).
 - [34] A. Rakonjac, A. Marchant, T. Billam, J. Helm, M. Yu, S. Gardiner, and S. Cornish, Phys. Rev. A **93**, 013607 (2016).
 - [35] S. J. Rooney, P. B. Blakie, and A. S. Bradley, Phys. Rev. A **86**, 053634 (2012).
 - [36] G. R. Dennis, J. J. Hope, and M. T. Johnsson, Comp. Phys. Comm. **184**, 201 (2013).
 - [37] P. K. Newton, *The N-Vortex Problem: Analytical Techniques*, Vol. 145 (Springer Science & Business Media, 2013).
 - [38] P. G. Saffman, *Vortex Dynamics* (Cambridge university press, 1992).
 - [39] H. Kober, *Dictionary of Conformal Representations*, Vol. 2 (Dover New York, 1957) p. 177.
 - [40] J. G. Esler, T. L. Ashbee, and N. R. McDonald, Phys. Rev. E **88**, 012109 (2013).

METHODS

Optically configured BECs. Our experimental apparatus consists of a ^{87}Rb BEC confined in a red-detuned laser sheet, providing harmonic trapping in the vertical z dimension with frequency $\omega_z = 2\pi \times 108$ Hz. The trapping in the x - y plane can be arbitrarily configured via direct projection of blue-detuned light which is patterned with a digital micromirror device (DMD) [31]. The BEC is formed using a hybrid optical and magnetic trapping technique[32]. We initially evaporate in a hybrid trap produced from a single, radially symmetric $95\text{ }\mu\text{m}$ waist 1064 nm red-detuned Gaussian beam and relaxed quadrupole magnetic field. Before reaching the BEC critical temperature, we transfer the atoms to a 1064 nm red-detuned Gaussian sheet and simultaneously ramp the magnetic field to zero. Optical evaporation over four seconds produces BECs of up to 3×10^6 atoms in the approximately azimuthally symmetric harmonic optical trap with $\{\omega_x, \omega_y, \omega_z\} = 2\pi \times \{6.8, 6.4, 360\}$ Hz. In the final second of evaporation, the 532 nm light illuminating the DMD is linearly ramped to a peak value of 10μ , where $\mu = k_B \cdot 22\text{ nK}$ is the chemical potential, producing a highly-oblate configured BEC with $N \sim 2.2 \times 10^6$ and $67(3)\%$ condensate fraction in a $125\text{ }\mu\text{m} \times 85\text{ }\mu\text{m}$ hard-walled elliptical trap. With the optical trapping beams held on, we levitate the cloud against gravity by ramping on an unbalanced quadrupole magnetic field, which additionally results in a 80 G DC residual magnetic field in the vertical direction. Simultaneously, we reduce the sheet trapping power resulting in the final trap frequencies $\{\omega_x, \omega_y, \omega_z\} \sim 2\pi \times \{1.8, 1.6, 108\}$ Hz, and trap depth of $\sim 90\text{ nK}$. We also reduce the DMD pattern depth to $\sim 5\mu$. Combined with the hard-walled confinement of the DMD, this results in an approximately uniform atom distribution with a calculated vertical Thomas-Fermi diameter of $6\text{ }\mu\text{m}$ and a healing length of $\xi \sim 500\text{ nm}$ at the centre of the trap (average $\xi \sim 530\text{ nm}$).

We measure the BEC lifetime in this trap to be $\sim 28\text{ s}$, which is shorter than the vacuum-limited lifetime of $\sim 60\text{ s}$. This suggests that scattering from the optical trap is a source of atom loss. We expect that a trap based on blue-detuned light would reduce this loss, and along with increased condensate fraction could potentially increase the lifetime of the vortex clusters.

For investigating vortex cluster energy damping as a function of BEC fraction, we arrest the evaporative cooling ramp, leading to an increased temperature and decreased condensate fraction. During the levitation procedure, due to the reduction in the optical dipole intensity and corresponding reduction in trap depth, we find loss of thermal atoms for the hotter conditions which occurs at a rate inefficient for continued evaporation. This results in an approximately constant $N_{\text{tot}} \sim 3.3 \times 10^6$ atoms in the final potential, while the final temperature and condensate fraction vary. The full range of temperatures and condensate fractions utilised were $T = \{23(1), 24(2), 27(1), 30(2), 31(2), 32.7(2)\}\text{ nK}$ and $N_c/N_{\text{tot}} = \{75.3(4), 67(3), 44(1), 33(1), 26(1), 18(2)\}\%$, respectively.

GPE simulations have also previously shown that increasing non-uniformity in the density of the condensate inhibits the dynamic formation of Onsager vortices [22]. To determine our sensitivity to this effect, we have increased the variation in the density of our BEC before performing the paddle sweep. This

is achieved by increasing the size of our trap while maintaining its aspect ratio, which increases the relative contribution of the residual harmonic optical trap from the optical dipole sheet potential to the 2D confinement. We examined two larger trap sizes, $140\text{ }\mu\text{m} \times 100\text{ }\mu\text{m}$ and $160\text{ }\mu\text{m} \times 115\text{ }\mu\text{m}$, and find that increasing the density variation leads to less concentrated vortex clusters as shown in Supplementary Fig. S3a, and increased energy damping, Supplementary Fig. S3b. For the larger $140\text{ }\mu\text{m} \times 100\text{ }\mu\text{m}$ trap, the temperature and condensate fraction was $T = 29(2)\text{ nK}$ and $N_c/N_{\text{tot}} = 75.1(3)\%$, while the $160\text{ }\mu\text{m} \times 115\text{ }\mu\text{m}$ trap had $T = 36(4)\text{ nK}$ and $N_c/N_{\text{tot}} = 71(1)\%$.

Obstacle sweeps. The paddle and grid obstacles are formed using the DMD. To dynamically alter the potential we upload multiple frames to the DMD, with the initial frame being the empty elliptical trap. Elliptical-shaped paddles, with a major and minor axis of $85\text{ }\mu\text{m}$ and $2\text{ }\mu\text{m}$ respectively, are then swept through the BEC at constant velocity. The paddle sweeps are defined by a set of 250 frames and the barriers start just outside the ellipse edge, with the paddles intersecting the edges of the elliptical trap at their midpoints. A $150\text{ }\mu\text{m/s}$ sweep ($\sim 0.1c$, where the speed of sound $c \sim 1290\text{ }\mu\text{m/s}$) is utilised for the $120\text{ }\mu\text{m} \times 85\text{ }\mu\text{m}$ trap, which results in a sweep time of 580 ms . Sequential paddle positions are separated by $\sim 350\text{ nm}$ resulting in smooth translation. After crossing the halfway point, the paddles are linearly ramped to zero intensity by reducing the major and minor axes widths to zero DMD pixels. For the larger elliptical traps, the paddle sizes are proportionately scaled. A $150\text{ }\mu\text{m/s}$ paddle sweep is maintained for the $140\text{ }\mu\text{m} \times 100\text{ }\mu\text{m}$ trap, but a $136\text{ }\mu\text{m/s}$ velocity is used to produce a similar number of vortices for the $160\text{ }\mu\text{m} \times 115\text{ }\mu\text{m}$ trap. For the grid case, an array of seven $4.5\text{ }\mu\text{m} \times 4.5\text{ }\mu\text{m}$ barriers were swept at $390\text{ }\mu\text{m/s}$, due to the increased critical velocity for vortex shedding, and then were similarly ramped to zero after crossing the halfway point.

BEC imaging and vortex detection. For darkground Faraday imaging [33] we utilise light detuned by 220 MHz from the ^{87}Rb $|F=1\rangle \rightarrow |F'=2\rangle$ transition in a 80 G magnetic field with $52.6\times$ magnification. This results in images with a measured resolution of $960(80)\text{ nm}$ FWHM at 780 nm illumination [31]. The $\xi \sim 500\text{ nm}$ healing length results in poor vortex visibility *in situ*, see Fig 2a,d. For the small phase shifts imparted by our vertically-thin cloud, raw Faraday images return a signal $\propto n_0^2$ which improves vortex visibility, after a short 3 ms time-of-flight (TOF), Fig. 2b,e. The density can be determined through postprocessing, Fig. 2a,d. However, Faraday imaging combined with a short 3 ms time of flight (TOF), where the optical beams are suddenly turned off, but the levitation field is held on, improves the vortex visibility significantly, while the column density is otherwise essentially unchanged, see Fig 2b,e. Vortices are detected automatically using a Gaussian blob vortex image processing algorithm [34] that examines connected regions of a thresholded background-subtracted image, after masking the image with the elliptical pattern, see Supplementary Fig. S1. We restrict detection of vortices to the inner 89% of the ellipse to avoid spurious detections on the condensate edge.

Effective 2D theory. Our oblate atomic BEC can be modelled

by the Gross-Pitaevskii equation (GPE)

$$i\hbar\partial_t\Psi(\mathbf{r},t) = \left[-\frac{\hbar^2\nabla^2}{2m} + V(\mathbf{r},t) + g|\Psi|^2 - \mu \right] \Psi(\mathbf{r},t), \quad (2)$$

where the interaction parameter $g = 4\pi\hbar^2 a_s/m$ for s-wave scattering length a_s and atomic mass m , and where μ is the chemical potential. To characterize the groundstate, the trapping potential $V(\mathbf{r})$ can be modelled as harmonic axial confinement and a hard-wall DMD potential in the x - y plane

$$V(\mathbf{r}) = V(z) + V(x,y) = \frac{1}{2}m\omega_z^2 z^2 + V_0 \Theta\left(\frac{x^2}{a^2} + \frac{y^2}{b^2} - 1\right), \quad (3)$$

where $\Theta(x)$ is the Heaviside function and $V_0 \gg \mu$. In the Thomas-Fermi approximation, the chemical potential of the groundstate is thus given by

$$\mu = \frac{1}{2} \left(\frac{3gN(m\omega_z^2)^{1/2}}{2\pi ab} \right)^{2/3}, \text{ i.e., } \mu \sim N^{2/3}. \quad (4)$$

To obtain an effective 2D theory, in the usual way we write $\Psi(\mathbf{r},t) = \psi(x,y,t)\phi(z)$. However, as the confinement in z is not strong enough to completely confine the wavefunction to the harmonic oscillator ground state, $\phi(z)$ is taken to be the Thomas-Fermi profile: $\phi(z) = (3g/4\mu l_z)^{1/2} \sqrt{(\mu - V(z))/g}$, where $l_z = (2\mu/m\omega_z^2)^{1/2}$ is the axial Thomas Fermi radius, such that $\phi(z)$ satisfies $\int dz |\phi(z)|^2 = 1$ and $\int d^2\mathbf{x} |\psi(x,y)|^2 = N$. Multiplying by $\phi^*(z)$ and integrating over z yields an effective 2D equation of motion

$$i\hbar\partial_t\psi = \left[-\frac{\hbar^2}{2m}(\partial_x^2 + \partial_y^2) + V(x,y) + g_2|\psi|^2 - \mu_{2D} \right] \psi, \quad (5)$$

where effective 2D interaction strength is $g_2 = 3g/5l_z$ and $\mu_{2D} = 4\mu/5$. For the BEC of 2.25×10^6 atoms in the $120 \mu\text{m} \times 85 \mu\text{m}$ trap, we obtain $\mu_{2D}/k_B = n_0 g_2/k_B = 19.63 \text{ nK}$, $\xi = \hbar/\sqrt{m\mu_{2D}} \approx 0.533 \mu\text{m}$ and $c = \sqrt{\mu_{2D}/m} \approx 1370 \mu\text{m/s}$. Values for the systems with lower condensate fraction or larger trap size are obtained by a simple scaling. Scaling the condensate number $N \rightarrow \alpha N$ gives $\xi \rightarrow \alpha^{-1/3}\xi$ and $c \rightarrow \alpha^{1/3}c$ while scaling the trap $\{a,b\} \rightarrow \lambda\{a,b\}$ yields $\xi \rightarrow \lambda^{2/3}\xi$ and $c \rightarrow \lambda^{-2/3}c$.

Dynamical modelling. We model the dynamical evolution of the experiment using phenomenologically damped GPE to account for energy and atom losses. Eq. (5) becomes

$$i\hbar\partial_t\psi = (1 - i\gamma) \left[-\frac{\hbar^2\nabla^2}{2m} + V(x,y,t) + g_2|\psi|^2 - \mu(t) \right] \psi, \quad (6)$$

where γ is the dissipation coefficient. Up to a noise term, Eq. (6) is equivalent to the simple growth stochastic Gross Pitaevskii equation (SGPE), a microscopically justified model of atomic BECs that incorporates dissipation due to interactions with a thermal component [35]. The exponential decay of the atom number, $N(t) = N_0 \exp(-t/\tau)$, for the decay constant $\tau \approx 28 \pm 2 \text{ s}$, is incorporated via a time-dependent chemical

potential $\mu(t)$. By Eq. (4) this gives $\mu(t) = \mu_{2D} \exp(-2t/3\tau)$. Empirically we find that the experimental data are well matched by numerical simulations with a dissipation coefficient of $\gamma = 8.5 \times 10^{-4}$. The total external potential is modelled as a combination of a stationary trap and time-dependent stirring obstacles: $V(x,y,t) = V_{\text{trap}}(x,y) + V_{\text{ob}}(x,y,t)$. The stationary component of the trap includes the optical dipole trap in the x - y plane, and binary DMD pattern convolved with the previously measured point spread function of the optical system [31]. The stirring obstacles are modelled by steep-walled hyperbolic tangent functions, which ramp up over a scale $\sim \xi$. The barrier sweep generates almost no compressible excitations (sound), and the kinetic energy injected into the condensate is almost entirely due to vortices.

The numerical simulations were performed using XMDS2 [36], using a Fourier pseudospectral method and an adaptive 4th-5th order Runge-Kutta time stepping scheme. The vortex positions \mathbf{r}_j are determined by numerically computing the curl of the superfluid velocity field, $\boldsymbol{\omega} = \nabla \times \hbar \nabla \theta / m = \Gamma \sum \kappa_j \delta(\mathbf{r} - \mathbf{r}_j)$, where $\kappa_j = \pm 1$ are vortex charges, $\Gamma = h/m$ is the quantum of circulation, and θ is the phase of the condensate wavefunction ($\psi = \sqrt{n}e^{i\theta}$).

Point-vortex energy. The point-vortex Hamiltonian can be solved in any simply connected domain using a conformal map to the unit disc, combined with the method of images. Under a conformal map $\zeta = f(z)$, which derives the vortex motion in the domain $z \in \Omega$ from that in the domain $\zeta \in \mathcal{D}$, the Hamiltonians are related via [37, 38]

$$H_\Omega(z_1, \dots, z_N) = H_{\mathcal{D}}(\zeta_1, \dots, \zeta_N) - \sum_{j=1}^N \kappa_j^2 \log \left| \frac{d\zeta}{dz} \right|_{z=z_j}, \quad (7)$$

where $z_j = x_j + iy_j$ is the complex position of the j th vortex. Note that the energy in Eq. (7) is dimensionless; physical energies can be obtained by multiplying by the energy unit $E_0 = \rho_0 \Gamma^2 / 4\pi$, where $\rho_0 = mn_0$ is the background superfluid mass density. If the map $\zeta = f(z)$ transforms a (simply connected) domain Ω to the unit disk $\mathcal{D} = \{\zeta \in \mathbb{C} \mid |\zeta| \leq 1\}$, Eq. (7) gives [37]

$$H_\Omega = -\sum_j \kappa_j^2 \log \left| \frac{\zeta'(z_j)}{1-|\zeta_j|^2} \right| - \sum_{j,k} \kappa_j \kappa_k \log \left| \frac{\zeta_j - \zeta_k}{1 - \zeta_j \zeta_k^*} \right|, \quad (8)$$

where $\zeta_j \equiv f(z_j)$ and the prime on the second sum indicates the exclusion of the term $j = k$. The domain of the ellipse interior, $\Omega = \{z \in \mathbb{C} \mid \Re(z)^2/a^2 + \Im(z)^2/b^2 \leq 1\}$ is mapped to the unit disk by the conformal map [39]

$$\zeta = f(z) = \sqrt{k} \operatorname{sn} \left(\frac{2K(k)}{\pi} \sin^{-1} \left(\frac{z}{\sqrt{a^2 - b^2}} \right); k \right). \quad (9)$$

Here $\operatorname{sn}(z; k)$ is the Jacobi elliptic sine function, $K(k)$ is the complete elliptic integral of the first kind, and k is the elliptical modulus, given by

$$k^2 = 16\rho \prod_{n=1}^{\infty} \left(\frac{1 + \rho^{2n}}{1 + \rho^{2n-1}} \right)^8, \quad (10)$$

where $\rho = (a - b)^2 / (a + b)^2$.

Calculation of entropy. To generate the entropy vs. energy curve, $S(E)$, in the elliptical domain in Fig. 1, we generate a histogram from 10^9 uniformly random, neutral configurations of $N = 18$ vortices within the ellipse, and calculate the energy for each state via the conformal mapping Eq. (8). We then take a histogram to determine the density of states, $W(E) = \int \prod_{i=1}^N d^2\mathbf{r}_i \delta(E - H(\{\mathbf{r}_i\}))$, which determines the entropy $S = k_B \log W$, where k_B is the Boltzmann constant. We calculate the energy from the vortex locations in terms of the 2D healing length $\xi = \hbar/\sqrt{mn_0g_2}$. Since the energy in Eq. (8) is defined up to an arbitrary additive constant, to simplify the comparisons between different data sets we then estimate the location of the structure function peak from a skewed gaussian fit to the numerically determined structure function and subtract off this value, such that negative (positive) energies correspond to positive (negative) temperatures in all cases.

Energy decay for varying BEC and trap parameters. As the total atom number N_{tot} is approximately constant, varying the BEC fraction and trap size leads to varying healing lengths, which we scale appropriately. We furthermore determine the density of states $W(E)$ for $N_{\pm} = 9$ vortices to determine the peak value for each healing length, and shift the energies as above. We then fit the energy decay with the function $E(t)/N = ae^{-t/\tau} + h_0$, where h_0 is a constant determined by a preliminary fit.

To test of the reliability of inferring the vortex circulations based solely on their position, we have also numerically generated a random (unclustered) ensembles of $N_{\pm} = 8$ vortices, equal to the mean number of vortices detected within the 89% detection region. We then calculate the energy of the configuration assuming that all vortices on the upper (lower) sides of the ellipse have positive (negative) circulation. This energy is indicated in the inset of Fig. 4b as a horizontal shaded regions, representing a 95% confidence intervals corresponding to the 10 samples at each hold time ($\pm 1.96\sigma/\sqrt{10}$). For the times the experimentally estimated vortex energy is larger than this value, we are confident that the vortices remain clustered despite the loss of vortex energy.

The decay fit for the largest $160 \mu\text{m} \times 115 \mu\text{m}$ trap (Supplementary Fig. S3b inset) tends towards an energy value above the uncorrelated estimate. We speculate, along with histogram (Supplementary Fig. S3a), that this may indicate the presence of a monopole state, consisting of a central like-circulation cluster surrounded by opposite circulation vortices and possessing net angular momentum. In a weakly elliptical trap this state

will have a comparable entropy to the (maximal entropy) dipole configuration [40].

Upper bound of the dipole moment– Considering two point vortices with opposite circulations in the elliptical domain, the mechanical equilibrium condition reads

$$0 = \kappa_i \frac{dx_i}{dt} = \frac{\partial H_{\Omega}}{\partial y_i}; \quad 0 = \kappa_i \frac{dy_i}{dt} = -\frac{\partial H_{\Omega}}{\partial x_i}, \quad (11)$$

where $i = 1, 2$, giving that $y_1 = y_2 = 0$ and $x_1 = -x_2 = d$ is the unique stationary point where the forces on each vortex due to the other vortex and the image vortices all cancel. Numerically solving Eq. (11), we obtain that $d \simeq 0.47a$.

Onset of the clustering. For an incompressible flow, one can introduce a stream function ψ to describe the flow, connected to the vorticity ω via $-\nabla^2\psi = \omega$. The self-consistent micro-canonical equation of the stream function of a system containing a large number of vortices in a bounded domain Ω is [6]

$$-\nabla^2\psi = \exp(-\tilde{\beta}\psi + \mu_+) - \exp(\tilde{\beta}\psi + \mu_-), \quad (12)$$

where μ_{\pm} are fixed by the normalisation conditions of vortex number densities, and $\tilde{\beta} \equiv (E_0N/2k_BT)$ is the inverse temperature in the natural energy units of the vortex system. Linearising Eq. (12) around the uniform state of vortices $\psi = 0$ and $n_0 = 2/A$ inside the area A , the fluctuation $\delta\psi$ satisfies

$$(\nabla^2 + \lambda)\delta\psi = 0, \quad (13)$$

with the Dirichlet boundary condition $\delta\psi(\mathbf{r} \in \partial\Omega) = 0$, here $\lambda = -4\pi\tilde{\beta}n_0$. The onset of the vortex clustering (purple star in Fig. 1d) occurs if Eq. (13) has nonzero solutions to the eigenvalue problem of the Laplacian operator in the elliptical domain [15]. In terms of elliptical coordinates Eq. (13) becomes Mathieu's equation. The most relevant eigenvalue associated with the transition is $\lambda = 4h^2/(a^2 - b^2)$, where h is the first positive root of the modified Mathieu function $\text{Mc1}(m, R, h)$ with $m = 1$ and $R = \tanh^{-1}(b/a)$. The transition happens at $\tilde{\beta} = \tilde{\beta}_c = -\lambda/(4\pi n_0) \simeq -1.614$, giving $T_c = (k_B\tilde{\beta}_c)^{-1}E_0N/2 \simeq -0.62T_0$, with $T_0 = E_0N/2k_B$.

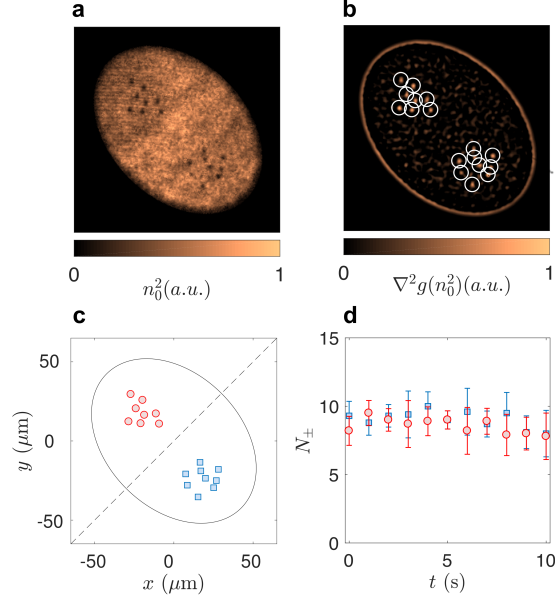


FIG. S1. **Vortex fitting and classification** – **a**, Background-subtracted Faraday image of the experimental BEC column density. **b**, The Gaussian blob algorithm takes the Laplacian of the Gaussian-filtered image to locate the vortex cores. **c**, Vortex circulations are then assigned across the minor axis, with positive vortices indicated by red circles and negative vortices indicated by blue circles. **d**, The distribution of positive and negative assigned vortices as a function of time for the data sets corresponding to Fig. 3a. Nearly equal numbers of positive and negative vortices are obtained throughout the hold times. The error bars indicate the standard deviation of the data.

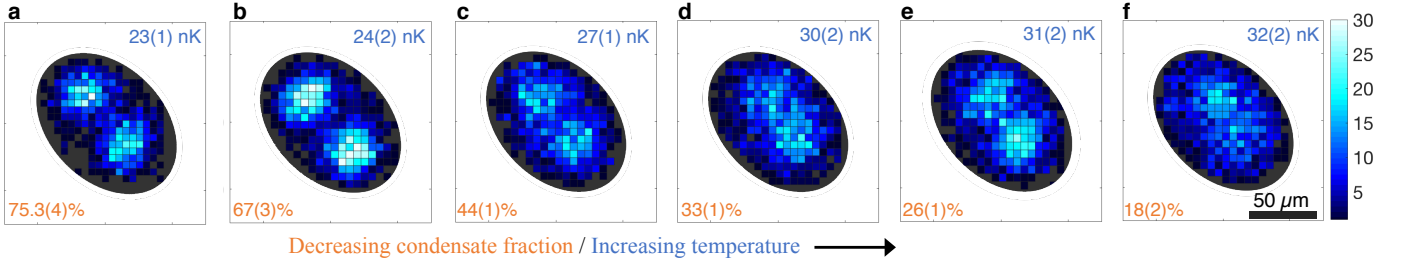


FIG. S2. **a – f**, Vortex position histograms corresponding to the full condensate fraction and temperature range in the $120 \mu\text{m} \times 85 \mu\text{m}$ trap considered in Fig. 4 of the main text. The initial condensate fraction is indicated in the bottom left, and the temperature in the top right of each subfigure.

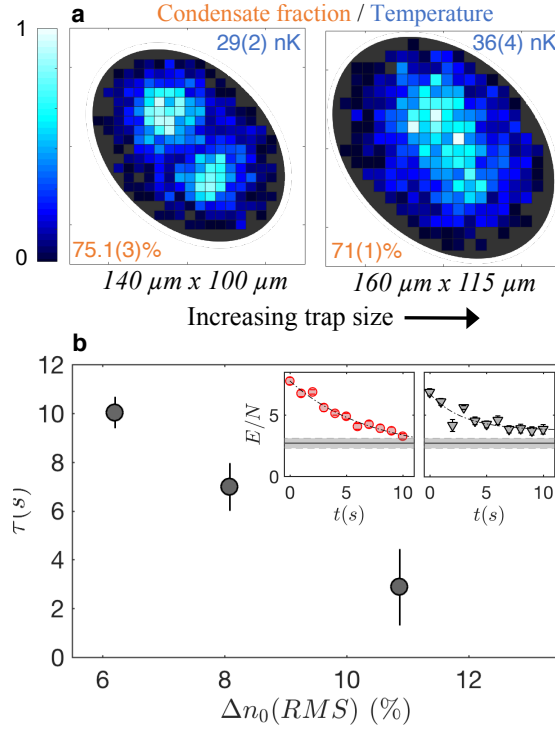


FIG. S3. **Metastability of Onsager vortex clusters with increased density variation.** **a** Cumulative vortex histograms over a 10 second for the intermediate $140 \mu\text{m} \times 100 \mu\text{m}$ and largest $160 \mu\text{m} \times 115 \mu\text{m}$ traps. **b**, The lifetime τ of the vortex energy as a function of BEC density variation, where the leftmost point corresponds to the $120 \mu\text{m} \times 85 \mu\text{m}$ trap which was utilised for the results presented in the main text. (inset) The decay of the vortex energy for the intermediate (red circles) and largest (black triangles) traps. The shaded region indicates the upper bound of the vortex configuration energy if our circulation allocation algorithm was applied to a random vortex ensemble (see text), and fits to an offset exponential decay are shown with dash-dot lines, determining the lifetime.

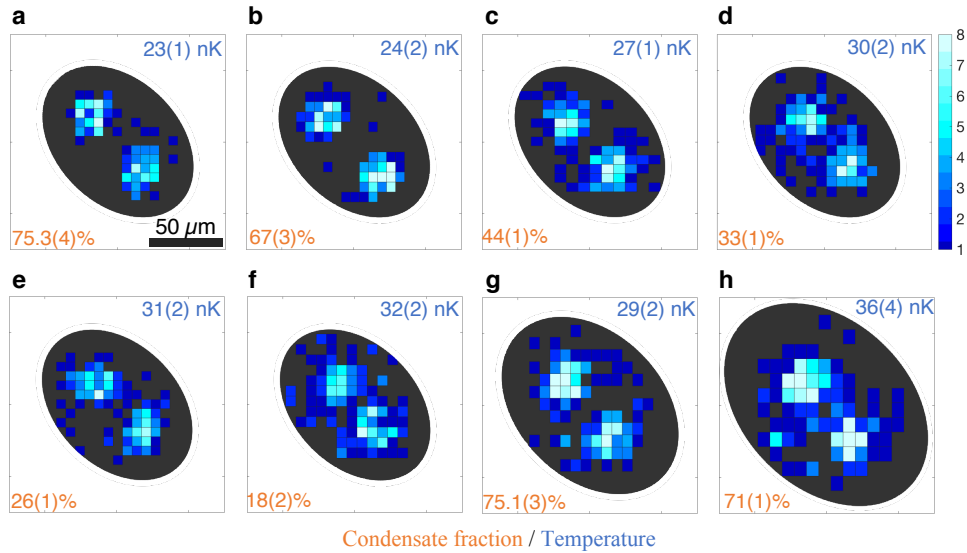


FIG. S4. **Initial vortex histograms immediately after the sweep.** **a – f**, Vortex position histograms corresponding to the full condensate fraction and temperature range in the $120 \mu\text{m} \times 85 \mu\text{m}$ trap considered in Fig. 4 of the main text. **g,h** Vortex position histograms for the $140 \mu\text{m} \times 100 \mu\text{m}$ trap, and the $160 \mu\text{m} \times 115 \mu\text{m}$ trap. The initial condensate fraction is indicated in the bottom left, and the temperature in the top right of each subfigure.

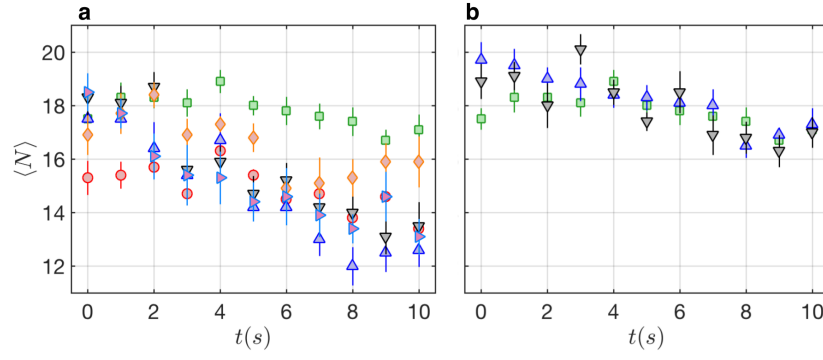


FIG. S5. **Mean vortex number as a function of hold time.** **a**, Vortex numbers as a function of time for different condensate fractions: 75.3(4)% (red circles), 67(3)% (green squares), 44(1)% (blue upward facing triangles), 33(1)% (black downward facing triangles), 26(1)% (orange diamonds), 18(2)% (red right facing triangles). **b**, Vortex numbers as a function of time for the larger traps, with larger condensate density variations: 120 $\mu\text{m} \times 85 \mu\text{m}$ trap and 67(3)% fraction (green squares), 140 $\mu\text{m} \times 100 \mu\text{m}$ trap (blue upward triangles), and 160 $\mu\text{m} \times 115 \mu\text{m}$ trap (black downward triangles).